LAWRENCE
LIVERMORE
NATIONAL
LABORATORY

LLNL-PROC-539271

Multi-layer predictive control for tomographic wavefront estimation

S. Mark Ammons, L. Johnson, R. Kupke, D. Gavel, C. Max, L. Poyneer

March 19, 2012

Adaptive Optics for Extremely Large Telescopes 2
Victoria, Canada
September 25, 2011 through September 30, 2011

Disclaimer

Multi-layer predictive control for tomographic wavefront estimation

S. Mark Ammons[1a], Luke Johnson[2], Renate Kupke[3], Donald T. Gavel[3], Claire E. Max, and Lisa A. Poyneer[1]

[1] Lawrence Livermore National Laboratory, Physics Division L-210, 7000 East Ave., Livermore CA 94550
[2] National Solar Observatory, 950 N. Cherry Ave., Tucson, AZ 85719
[3] Center for Adaptive Optics, University of California, Santa Cruz, 1156 High St., Santa Cruz, CA 95064

Abstract. We discuss the extension of predictive control techniques utilizing Taylor frozen-flow motion to multi-guide star, multi-layer tomographic wavefront measurement systems. The expectation is that the combination of height information from multiple guide stars and wind velocity estimates breaks degeneracies in volumetric phase reconstruction, particularly for voxels sampled by only one GS, allowing for a reduction of the tomographic error and an expansion of the field of view. Using a simple shifting-and-averaging scheme to track individual layer motions in simulation, we demonstrate 3-10% reductions in the tomographic wavefront estimation error of individual layers for an aperture size of 10 meters, subapertures of 30 cm, a Mauna-Kea type atmospheric profile, and wind velocities of 10 m/s. The majority of the benefits occur in regions sampled by only 1-2 LGS's downwind at high altitudes. An idealized scenario with 100% Taylor frozen-flow motion, perfect knowledge of wind velocities, and noise-free wavefront sensors is assumed.

1 Introduction

The development of the Sodium Laser Guide Star (LGS) as a point source reference for astronomical adaptive optics systems [4,9,12,13] has opened new frontiers for near-infrared science at the diffraction-limit. These gains have largely been driven by the increased sky coverage available with LGS-AO compared to Natural Guide Star (NGS) AO Systems. However, there are several disadvantages of laser guide stars that prevent LGS-AO systems from achieving the kind of wavefront quality that NGS-AO systems can deliver for stars of equivalent photon flux, including LGS elongation, a large LGS spot size, and the cone effect.

The *cone effect* refers to an error in estimating the phase integrated through a cylinder of turbulence using a laser guide star, which illuminates a cone of turbulence. As a result of this geometric mismatch, there are turbulent regions outside of the LGS cone that remain unsensed and uncorrected for distant sources. One potential solution to the cone effect is to use multiple laser guide stars in a constellation that completely fills a cylinder of turbulence (Figure 1, left panel). To compute the integrated wavefront to a science object in a multi-LGS system, the measured LGS wavefronts must be analyzed tomographically [17,19,18]. *Tomography* here refers to a reconstruction of the three-dimensional distribution of turbulent phase in a volume using phase integrals in several directions as input. Rays must then be forward-propagated through the reconstructed medium to predict the integrated wavefront in object directions [5]. The term *Laser Tomographic Adaptive Optics* (LTAO) encompasses a range of AO architectures that use multiple laser guide stars with tomography to access wider corrected fields of view (e.g., Figure 1, right panel) or to achieve more accurate wavefront estimation. Other publications go into further detail about various types of LTAO [3,1,2].

Tomographic wavefront estimation is subject to a number of errors, including errors stemming from misestimation of the LGS positions, atmospheric layer heights or strengths [6]. For the purposes of these proceedings, we will be concerned with the tomographic error due to blind modes, which remains even in the presence of noise-free wavefront sensing and perfect knowledge of the LGS constellation and C_N^2 distribution. This error is dependent only on the geometry of the LGS/telescope

[a] ammons1@llnl.gov

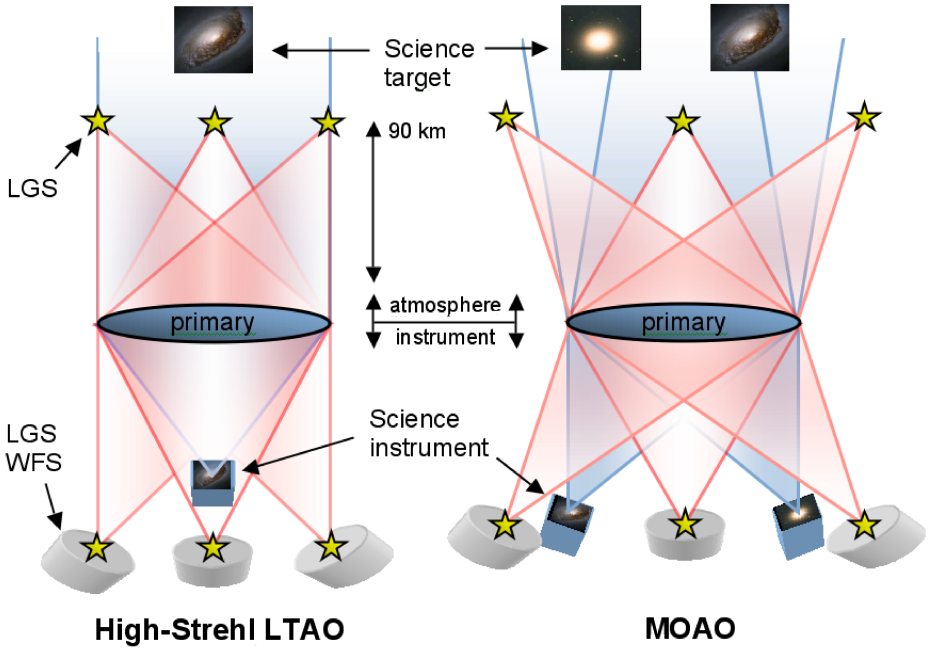

Fig. 1. Schematic of Laser Tomographic Adaptive Optics architectures. Yellow stars denote laser guide stars and red lines indicate the optical paths of LGS rays. Blue lines indicate paths traced by light from science targets. Left panel: LGS constellation is designed to provide complete wavefront sensing of a cylindrical region. Right panel: LGS constellation is expanded to achieve a wider field of view, but with a penalty of increased tomographic error. Reproduced from reference [1].

arrangement and the C_N^2 profile. This error increases as the number of laser guide stars is decreased and their separation increases. The tomographic error can be the dominant error budget term, as it is in some existing system designs [14], limiting the Strehls and field sizes obtainable with LTAO systems. Yet, since it is driven by LGS number and areal density, it is closely tied to the expense of such systems. Techniques that improve tomographic wavefront estimation for a given LGS constellation will be important for pushing LTAO to bluer wavelengths and wider fields.

In these proceedings, we investigate multi-layer predictive wavefront control under the assumption of Taylor-frozen flow as a technique to reduce the tomographic error due to blind modes. Using a simulator of atmospheric tomography with a simplistic LGS geometry and noiseless wavefront sensors, we show that wavefront estimation of individual moving layers at different atmospheric heights can be improved with a simple shift-and-average scheme. The reader is cautioned that these experimental results are obtained under a set of ideal conditions and are offered as an "existence proof" only that tomographic wavefront estimation errors may be improved with predictive schemes. Future work will test this idea under a more realistic range of assumptions. In these proceedings, only cursory references to the extensive literature on predictive control and tomographic adaptive optics are made, and we regret unintentional omissions of relevant studies. Section 2 presents a short introduction to predictive wavefront control. Section 3 describes the setup of the tomographic simulator and Section 4 presents results and concludes.

2 Predictive Wavefront Control Utilizing Taylor Frozen-Flow Motion

Predictive wavefront control takes advantage of Taylor frozen-flow motion of atmospheric components to predict the wavefront at later time steps [15, 10, 16, 11]. Controlling for wind in this manner

averages over multiple previous time steps, reducing the effects of random components of wavefront noise induced by photon errors or detector noise without sacrificing bandwidth. For an atmosphere with at least some contribution from Taylor frozen flow, the moving component may be pre-shifted to compensate for known time delays between sensing and correction. The advantages of predictive wavefront control assuming Taylor frozen flow have been characterized [15, 11] and frozen flow has been observed at a variety of locations [15, 16].

We now consider the extension of predictive control to a multi-layer, tomographic AO architecture. Our working model is that each atmospheric layer has an independent wind velocity and direction and is located at a different atmospheric height. As tomographic error is determined by the vertical arrangement of phase, it is plausible that the error modes at each layer become decorrelated in time as the layers translate in different directions. If this were the case (i.e., tomographic error at a given layer does not translate with the layer), an improved estimate of the atmospheric layer could be obtained by simply averaging shifted phase over multiple time steps according to the estimated wind velocity and direction.

Irregardless of whether multi-layer predictive control could improve tomography internal to the LGS constellation, it is also plausible that wavefronts could be estimated beyond the radius of the LGS constellation as the phase translates into regions of the metapupil sampled by only one LGS. In these regions, no information about the height of the measured phase is obtainable by tomography alone, and therefore the integrated phase is difficult to predict at other field points. In a multi-layer scenario in which each layer has a different height and wind vector, phase measured in well-sampled regions of the metapupil (with low tomographic error) eventually translates into regions sampled by only one LGS, giving critical information about the height of the phase. Thus, with this information, the integrated phase can be predicted at other field points if it can be tracked layer-by-layer.

3 Experimental Setup

We now introduce a simple experiment to test the concept that, in an ideal, noise-free situation, multi-layer wind predictive control can improve our ability to estimate the phase in individual atmospheric layers. To reduce the effects of other tomographic errors resulting from C_N^2 or layer height misestimation, we constrain the model atmosphere to have the same number of layers and layer heights as the true atmosphere. We use a simple shift-and-average scheme (described in Section 3.2) to estimate the moving average of phase in each layer, assuming perfect knowledge of wind vectors. For this experiment, all wavefront measurement is assumed to be open-loop, as is typically the case for LTAO and MOAO designs.

3.1 Tomographic Simulator

We use the TomographySphericalWave (TSW) simulator, which performs back-projection tomography in the Fourier domain for finite apertures [7]. This iterative algorithm computes a least-squares solution to the tomography problem $\mathbf{y} = \mathbf{A}\mathbf{x}$, where $\mathbf{x}$ is a vector of phase "voxels" within the volume, $\mathbf{y}$ is the vector of wavefront measurement samples, and A is interpreted as a "forward-propagation" matrix that forms lines integrals of $\mathbf{x}$ through the volume [8]. The solution takes the form:

$$\mathbf{v}_{k+1} = \mathbf{v}_k + \Delta\mathbf{v}_k \tag{1}$$

$$\Delta\mathbf{v}_k = a\mathbf{C}\mathbf{e}_k \tag{2}$$

$$\mathbf{e}_k = \mathbf{y} - (\mathbf{A}\mathbf{P}\mathbf{A}^T + \mathbf{N})\,\mathbf{v}_k \tag{3}$$

$$\mathbf{x} = \mathbf{P}\mathbf{A}^T\mathbf{v}_\infty \tag{4}$$

where $\mathbf{C}$ is a diagonal pre-conditioning matrix, $\mathbf{P}$ and $\mathbf{N}$ are diagonal post-conditioning matrices, and a is a constant chosen to keep the iteration process stable. This procedure converges to the solution

$$\mathbf{x} = \mathbf{P}\mathbf{A}^T\,(\mathbf{A}\mathbf{P}\mathbf{A} + \mathbf{N})^{-1}\,\mathbf{y} \tag{5}$$

For this experiment, tomography is performed in phase units with no slope-to-phase conversion or noise in the wavefront sensors. All atmospheric spatial frequencies above Nyquist are removed from simulated phase screens before the tomographic iterations, essentially removing sampling and aliasing errors. True tip/tilt information is preserved on the LGS wavefronts. Twenty tomography iterations are computed for each AO time step with an iteration gain of $a = 0.25$.

The simulation assumes a 10-meter aperture, 30 cm subaperture size (33 subapertures across the pupil), and a circular constellation with 3 LGS's. Two different C_N^2 distributions are investigated in two separate cases. Each atmospheric realization is 833 milliseconds in length and 200 realizations are performed for each case. A 1 kHz frame rate is assumed. Other TSW and atmospheric parameters are summarized in Table 1. The average depistoned, detilted RMS difference between the forward-propagated volume and the measured LGS wavefronts after 20 tomography iterations is $\sim$ 20 nm, indicating reasonable convergence of the tomographic algorithm.

Table 1. Experimental Parameters for Tomography Spherical Wave. Values for three different layers are grouped in bracketed sets.

Parameter	Case 1	Case 2
$r_{0,500\ nm}$ (cm)	16	16
Telescope diameter (m)	10	10
Subaperture size (cm)	30	30
Number of layers	3	3
Layer heights (km)	[0,5,10]	[0,5,10]
C_N^2 distribution	[45%, 30% 25%]	[55%, 30% 15%]
LGS constellation diameter (“)	120	120
Wind Speed (m/s)	[10, 10, 10]	[10, 10, 10]
Wind Direction (degrees)	[+270, +180, +90]	[+270, +180, +90]
Simulation length (ms)	833.3	833.3
Number of atmospheric realizations	200	200
Frame rate (Hz)	1000	1000

3.2 Multi-Layer Shift-and-Average Technique

We use a simple shift-and-average scheme with unity gain to estimate and track the phase of a moving wind layer. Following the completion of the tomographic iterations in a time step, phase voxels at a physical location $(\mathbf{r}, t')$ (where $\mathbf{r}$ is a two-dimensional location vector in a given layer of height h and t' is the current iteration time) are replaced according to

$$\Phi'(\mathbf{r},\ t') = \frac{1}{n' - n_0 + 1} \sum_{n=n_0}^{n'} \Phi(\mathbf{r} - c(n' - n)\mathbf{v}, cn) \tag{6}$$

where n is the zero-indexed timestep number, n' is the current timestep number, c is the time interval between AO iterations (with $t = cn$), and $\mathbf{v}$ is the known wind velocity vector. The parameter n_0 is the timestep number at which averaging is started; for these experiments, $n_0 = 0$. The averaging is only performed over phase elements that are measured in a region of the metapupil *sampled by more than one LGS,* as the tomographic error is lowest in this region. Similarly, only phase elements *downwind* from this section of the metapupil are replaced. The modified volume estimate Φ' is only used to assess agreement with the true volume, and is neither used as a starting point for tomography in later timesteps nor to compute the average in eqn. (6) above.

4 Results and Discussion

The results of the experiment are tabulated in Table 2 and displayed in Figure 2. Table 2 shows the average on-axis tomographic error for each case, of order $\sim$ 200 nm for the wide constellations cho-

sen. The average RMS wavefront amplitude is also shown for each case. Of importance is the third row in Table 2, which shows the average percent improvement in RMS deviation between the true atmospheric phase and the estimated phase when using the shift-and-averaged predictive technique, compared to no prediction, for each layer. These measurements are taken at the end of each of 200 realizations ($t = 0.83s$). Note that, for each case and each layer, there is improvement in the overall estimation of the phase (i.e., the values are positive), with the exception of the ground layer in Case 2.

Figure 2 displays maps of percent improvement in the RMS deviation between true atmospheric phase and the estimated phase, averaged over 200 realizations. Each row corresponds to a different atmospheric case; each column corresponds to a different layer for a given case. These measurements are taken at the end of the simulation ($t = 0.83s$). In these maps, positive values correspond to regions of the metapupil that benefit from multi-layer predictive control. The red arrows show the directions of wind motion for each layer. Note that, in general, regions of positive improvement are found in downwind areas, indicating that the benefit is due solely to shifting-and-averaging. The majority of the benefit is seen in regions of the metapupil that are only sampled by one LGS. However, the results are mixed in both cases for the ground layer (3.1, -5.9%), in which no region of the metapupil is sampled by less than three LGS's. This implies that shifting-and-averaging provides the most benefit in sparsely-sampled regions and may not provide benefit in well-sampled regions.

Table 2. Summary of experimental results and derived parameters. Values for three different layers are grouped in bracketed sets. Results are averaged over 200 realizations.

Parameter	Case 1	Case 2
RMS on-axis time-averaged tomographic error (nm)	218	181
Average RMS wavefront amplitude in layer (nm)	[802,436,328]	[923,453,226]
Improvement in layer estimate after 0.83 s, with prediction	[3.1%,10.0%,3.3%]	[-5.9%,7.2%,3.2%]

In summary, these results suggest that even a simplistic predictive control scheme such as shifting-and-averaging can provide 3-10% relative benefits to wavefront estimation quality, when comparing estimated layer phase to true layer phase. The majority of the benefits occur in sparsely-sampled regions downwind at high altitudes. This effect was anticipated (see section 2), as the height of phase cannot be estimated in regions sampled by only one LGS, and tracking phase that moves into these regions effectively defines the height of the moving phase. However, mixed results for the ground layer imply that the tomographic error may not average down as the phase translates in regions sampled by 3 LGS's, which could mean that the tomographic error modes are not decorrelated with wind velocity. The reader is cautioned that these results are obtained for a highly idealized, noiseless set of cases, in which the tomographic error is not affected by C_N^2 errors or layer height misestimation, and the atmosphere is composed of pure frozen-flow motions whose wind vectors are known. Further simulation will verify the utility of more rigorous multi-layer predictive control techniques in real-world scenarios.

5 Acknowledgements

This work performed under the auspices of the U.S. Department of Energy by Lawrence Livermore National Laboratory under Contract DE-AC52-07NA27344 with document release number LLNL-PROC-539271.

References

1. Ammons, S.M., Johnson, L., Laag, E., Kupke, R., Gavel, D.T., Bauman, B.J., and Max, C.E., Publications of the Astronomical Society of the Pacific **122** (2010), 573.

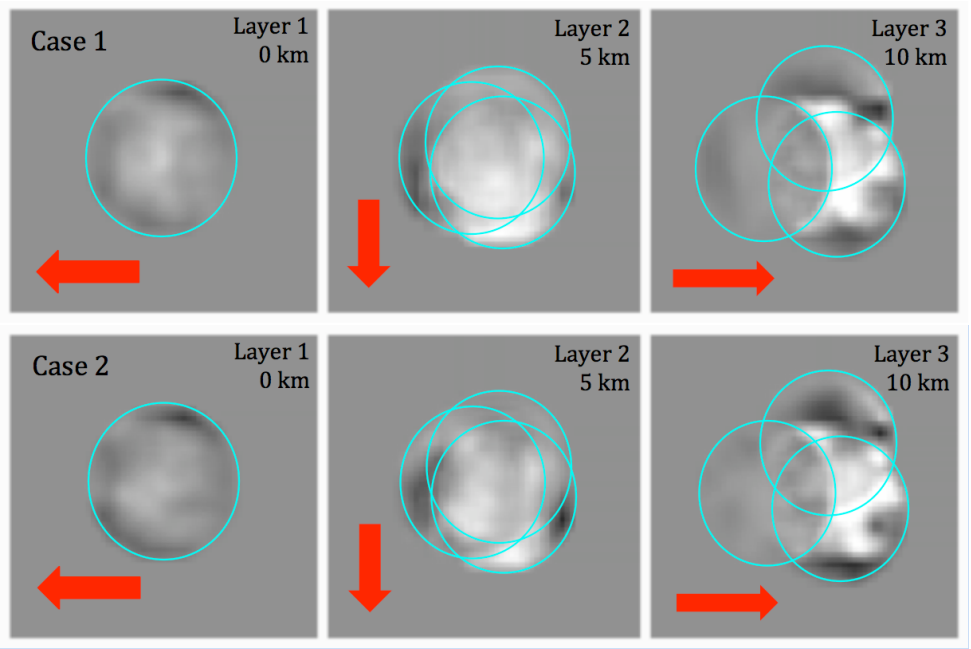

Fig. 2. Maps of percent improvement in the RMS deviation between true atmospheric phase and the estimated phase seen with shifting-and-averaging, averaged over 200 realizations. Maps are smoothed by two subapertures. The grayscale range is [-25%, +25%]. Each row corresponds to a different atmospheric case; each column corresponds to a different layer for a given case. These measurements are taken at the end of the simulation ($t = 0.83s$). The red arrows denote the directions of wind motion for each layer. Aquamarine circles mark the borders of metapupils for each case. In these maps, positive values correspond to regions of the metapupil that benefit from multi-layer predictive control. Note that larger benefits tend to appear downwind in regions sampled by only one or two LGS's in high-altitude layers.

2. Costille, A., Petit, C., Conan, J.-M., Kulcsar, C., Raynaud, H.-F., and Fusco, T., Journal of the Optical Society of America-A **27** (2010), 469.
3. Dekany, R.G., Britton, M.C., Gavel, D.T., Ellerbroek, B.L., Herriot, G., Max, C.E., and Veran, J.-P., proceedings of the SPIE **5490** (2004), 879.
4. Fugate, R., Fried, D., Ameer, G., Boeke, B., Browne, S., Roberts, P., Ruane, R., Tyler, G., and Wopat, L., Nature **353** (1991), 141.
5. Fusco, T., Conan, J., Rousset, G., Mugnier, L. M., and Michau, V. Journal of the Optical Society of America-A **18** (2001), 2527.
6. Fusco, T. and Costille, A, proceedings of the SPIE **7736** (2010), 17.
7. Gavel, D.T., proceedings of the SPIE **5490** (2004), 1356.
8. Gavel, D.T., Reinig, M., & Cabrera, C., proceedings of the SPIE **5903** (2005), 2.
9. Humphreys, R., Primmerman, C., Bradley, L., and Herrmann, J., Optics Letters **16** (1991), 1367.
10. Johnson, L., Gavel, D.T., Reinig, M., and Wiberg, D., proceedings of the SPIE **7015** (2008), 92.
11. Johnson, L., Gavel, D.T., and Wiberg, D., proceedings of the SPIE **7736** (2010), 92.
12. Lloyd-Hart, M., Angel, J., Jacobsen, B., Wittman, D., Dekany, R., McCarthy, D., Kibblewhite, E., Wild, W., Carter, B., and Beletic, J., Astrophysical Journal **439** (1995), 455.
13. Max, C.E., Olivier, S. S., Friedman, H. W., An, J., Avicola, K., Beeman, B. V., Bissinger, H. D., Brase, J.M., Erbert, G. V., Gavel, D. T., Kanz, K., Liu, M. C., Macintosh, B., Neeb, K. P., Patience, J., and Waltjen, K. E., Science **277** (1997), 1649.
14. Neyman, C. & Dekany, R., Keck Adaptive Optics Note **629** (2008), 1.
15. Poyneer, L.A. & Veran, J.-P., proceedings of the SPIE **7015** (2008), 36.

16. Poyneer, L.A., van Dam, M., & Veran, J.-P., Journal of the Optical Society of America-A **26** (2009), 833.
17. Ragazzoni, R., Marchetti, E., and Rigaut, F., Astronomy & Astrophysics **342** (1999), 53.
18. Tokovinin, A., Le Louarn, M., Viard, E., Hubin, N., and Conan, R., Astronomy & Astrophysics **378** (2001), 710.
19. Viard, E., Hubin, N.N., Le Louarn, M., Delabre, B., Monnet, G.J., and Tokovinin, A.A., proceedings of the SPIE **4007** (2000), 94.